High rate compressive behaviour of a dilatant polymeric foam

Kapil Bharadwaj Bhagavathula[1*], Austin Azar[1], Simon Ouellet[2], Sikhanda Satapathy[3], Christopher R Dennison[1] and James David Hogan[1*]

[1]Department of Mechanical Engineering, the University of Alberta, Edmonton, AB T6G 2R3, Canada.

[2]Valcartier Research Centre, Defence Research and Development Canada, Quebec, QC, G3J1X5, Canada.

[3]Soldier Protection Sciences Branch, U.S. Army Research Laboratory, Aberdeen Proving Ground, MD 21005, USA.

Abstract

Polymeric foams are an essential part of personal protection equipment, such as helmets and body armor. In this work, we study the strain-rate dependent behavior of a dilatant polymeric foam, focusing on developing characterization and testing methodologies needed to better understand the links between microstructure and failure in these materials. We study these links for a commercially-available shear-thickening foam, named D3O LITE D. Prior to testing, the pore sizes (82 ± 26 μm), ligament thickness between pores (5 to 12 μm), and porosity (83 ± 5 %) were quantified using Scanning Electron Microscope images. Samples were then tested in compression under quasi-static conditions for a strain rate of 0.04 s^{-1} using an MTS testing apparatus, and in dynamic conditions using a split Hopkinson pressure bar apparatus for strain rates of 5280 to 5720s^{-1}. For both rates, strains upwards of 85% were achieved and this allowed us to examine a variety of material failure behaviors, including elastic collapse, localization, pore collapse, densification and post pore collapse hardening. These mechanisms are observed in-situ during compression experiments using high-speed photography, and linked back to stress-strain responses of the materials. In this material, the elastic collapse stress for quasi-static and dynamic compression conditions was found to be 120 ± 40 kPa and 243 ± 47 kPa, respectively, and elastic

modulus were noted of 2.4 ± 0.7 MPa and 3.8 ± 1.2 MPa, respectively. Following the elastic collapse, some unique specimen-scale localization features were observed during the dynamic experiments. These features are unique to dynamic compression and were not observed for the quasi-static case, demonstrating a demonstrating a distinct high-rate behavior for this material, possibly linked to its "shear thickening" label. After densification, complete pore collapse followed by post pore collapse hardening were observed for both strain rates. These results represent some of the first studies on shear-thickening foams in the literature, and the testing methodologies developed in this study will serve as the foundation for additional experimental and computation studies across a broader range of foam materials.

1. Introduction

The ability to dissipate energy using foams is an aspect that has many engineering challenges in dynamic applications, such as Automotive Industry [24], core materials in composite sandwich constructions [16], and Personal Protective Equipment [8, 14 and 15]. Typical foam materials used in these energy-absorbing applications include Expanded Polystyrene (EPS) [21, 30 and 32], Expanded Polypropylene (EPP) [11, 32], and Thermal Polyurethanes (TPU) [8, 31]. These studies have focused on better understanding the effect of microstructure [11, 18, and 31], density [11, 18 and 32] and strain-rate [10, 11, 17, 18 and 30] in tension [22] and compression [17 - 25], as well as during impact experiments using drop testing [13] and gas-gun approaches [24]. In this paper, we investigate the rate-dependent compressive stress-strain response and failure of a polymeric foam, and so focus on presenting the limited literature in this area (specifically for the dynamic regime).

Split Hopkinson pressure bar (SHPB) is a widely recognized experimental technique used to investigate the strain-rate dependent response and stress-strain curves for a variety of soft

engineering materials at high strain rates from 10^2 to 10^5 s^{-1} [2, 9 and 16 – 19]. For example, Saha et al. [18] have shown that different grades of rigid polyurethane (PUR) foams and cross-linked polyvinyl chloride (PVC) foams exhibit some form of strain rate dependency. At quasi-static strain rates, both PUR and PVC foams show an increase of ~15% in yield and peak stresses with every increase in one order of magnitude of the strain rates from 0.001 s^{-1} to 0.1 s^{-1}. At strain rates above 700 s^{-1}, they observed a two-fold increase in the yield strengths, which were twice as much when compared to the quasi-static regime. They also observed that yield strengths remained constant with increasing strain rates up to 1700 s^{-1} and the only changes observed in the compressive response are at the peak stresses. Similarly, Ouellet et al. [17] performed studies at strain rates from 0.008 s^{-1} to 2700 s^{-1} and found that polystyrene foams exhibited noticeable strain rate dependency in stresses only at rates greater than 100 s^{-1}. Their paper also looked at polyethylene foams and found that these also exhibit rate dependency, but only at strains greater than 20%. In another paper, Song et al. [30] studied a different grade of polystyrene foam than Ouellet et al. [17] and found an increase of ~10% in collapse stress with every increase in the order of magnitude of the strain rates from 0.001 s^{-1} to 950 s^{-1}.

In many of these papers and other studies, the authors point to the importance of microstructure (usually in terms of density [11, 13 and 18] and cell sizes [11, 18 and 30]) and failure (usually through a post-test macroscopic assessment of the sample [17, 32 and 35]) on the strain-rate dependent behavior of polymeric foams. For example, Di Landro et al. [21] and Santa Maria et al. [20] suggested smaller cell sizes results in increased strength compared to larger cell sizes. They also noted an increase in the amount of energy that was absorbed (through measure of strain energy) at higher strain rates for smaller cell sizes and, consequently, higher relative densities [11, 18, and 21]. In addition to increases in strength and energy absorption behaviors for smaller cell

sizes, Bouix et al. [11] found that smaller cell sizes resulted in less sensitivity to increasing strain rate when compared with larger cell sizes. The importance of cell sizes on the rate dependent behavior of polymeric foams is coupled to onset and evolution of failure processes in these materials, and how these processes compete at different strain rates (e.g., work by Saha et al. [18]). Several failure mechanisms that have been studied for polymeric forms are the inertia [35], stretching and buckling of the cell walls [21], and the effects of trapped gases [11, 21]. Understanding these relationships between failure mechanisms, microstructure, and the strain-rate dependency of polymeric foams is important in order to develop improved materials in the future; this is what we begin to do in this paper.

Building upon these past works investigating effects of microstructure and failure on the strain-rate dependent behavior of polymeric foams, this paper investigates the high strain-rate deformation of dilatant foams that is advertised as "shear-thickening". This material is employed in both industrial and military applications where energy absorption qualities are desired. In this paper, we focus on beginning to understand the effect of pore size and wall thickness on the behavior of this shear-thickening foam for different strain rates. As limited work has been done in the published literature on shear thickening foam materials, this study intends to begin to establish an understanding of mechanical properties and dynamic behavior, accomplished through experimentation and characterization. The paper is comprised of the following sections: first, microstructure characterization techniques and sample preparation methods are established and described. Second, testing methods are presented, followed by the presentation of the experimental results. These results are supported by stress-strain curves and video images obtained from high-speed cameras. Finally, implications and contributions of this work are highlighted, and future directions are suggested.

2. Materials and Characterization

2.1. Material and sample preparation

The material investigated in this work is a semi-open/closed-cell polymer-based foam that was manufactured by D3O®. The variant under investigation is 'D3O® LITE D', which is advertised as a non-Newtonian shear-thickening material. To ensure consistency across strain-rates, a single sample size was used for both quasi-static and dynamic experiments. Common sample preparation techniques [17, 24] like the use of a hollow punch were initially adopted in this study. Other techniques for sample preparation were also pursued, including water-jet cutting and solid metal punch, but it was found that hollow punch technique results in the least amount of damage to the outer surface of the specimens. Using a special metallic hollow punch, disk samples of diameter 8 ± 0.3 mm were cut from an as-received sheet of uniform thickness of 4mm, with the axis of the disk oriented along the through-thickness direction of the as-received sheet of foam. Care was taken to ensure that the samples' end surfaces were parallel, and that minimum damage is induced to the edges during sample preparation. The choice of these sample size and shape resulted in constant strain-rate deformation and the best force equilibrium for the dynamic experiments, which are two criteria that are noted to be important and challenging when testing soft materials [3 – 5, 9] (results presented later in Figure 6 and 8).

The physical and mechanical properties provided by the manufacturer are listed in Table 1 [1]. We note that differences in the compressive strength between this study and those provided by the manufacturer is expected because the specimen sizes used in the ASTM D3575-14D is 25.4 mm x 25.4 mm x 25.4 mm, whereas the test specimen in our study is 8 mm in diameter and 4 mm in thickness (which is governed by the thickness of the as-received foam sheet). The sensitivity of material strengths to geometry and specimen-size effects are documented in the literature [11, 24],

including experiences by authors, and we expect that to manifest in differences in our strengths and those provided by the manufacture. Note, potential differences in composition, pore sizes and wall thicknesses may also occur as a consequence of different as-received sheet sizes.

2.2. Microstructure characterization

For 2-D microstructure characterization, a Hitachi S-4800 field emission scanning electron microscope (SEM) was used. Figure 1 (a) shows an SEM image of D3O® LITE D at 100x magnification. From this cross-sectional view, the pores appear to be fairly circular and it is observed that the microstructure is mostly dominated by closed cells with small regions of semi-open cell features. These semi-open cells are noted with red circles in Figure 1 (a), while the closed cells are more obvious. The concentrated bright features that appear near the cell wall boundaries, which lay inside the pore structures, are believed to be either small chunks of unexpanded polymer that remain intact during the cooling stage of manufacture process, or some form of additives that may have been introduced during the foaming process. Pore sizes were measured using ImageJ across the 10 SEM images (728 total pores), and were found to range between 50 and 200μm with an average pore size of 82 ± 26 μm. Image processing techniques developed by Hogan et al. [28] were used to compute the area fraction of the pores as a measure of porosity. The average porosity of the material was found to be 83 ± 5% across the 10 images that were used this computation.

Next, shown in Figure 1 (b) is an SEM micrograph of the material taken at a higher magnification of 600x. Using ImageJ, the wall thickness are computed across 10 images across the cross-section and wall thickness is estimated by measuring minimum thicknesses of the walls between adjacent pores. The average wall thickness across 10 images (750 total measurements) is calculated to be 8.3 ± 4.5μm, with wall thicknesses ranging between 5 and 12μm. Measurements of pore size and

wall thickness are used later when describing the effect of microstructure on the rate-dependent failure this foam.

3. Experimental Methods

3.1. Quasi-static compression

The specimens were tested at a quasi-static strain rate of 0.04 s^{-1} using a Material Test System (MTS) – 810 machine, a schematic of which is shown in Figure 2. This assembly included visualization capabilities with a AOS PROMON U750 – high-speed camera, which enabled us to observe macroscopic deformation features during testing. This camera has a resolution of 1280 x 1024 pixels and recorded at a framerate of 24 Frames per second (FPS), which coincided with the data acquisition rate of the MTS machine. Both camera and MTS were triggered manually at the same time, and the synchronization was verified through comparison between when the piston displacement was first observed in the camera images with the displacement data recorded by the MTS machine (no adjustments were necessary). To perform the test, the specimen is placed between a compressive grip of the MTS that consists of two 25.4 mm diameter steel bars (Figure 2). These are guided and held with precise alignment. A cylindrical piston, moving at a constant displacement rate is used to compress the samples. A 10 kN load cell with a background noise corresponding to approximately ±1 N recorded the time histories of the forces, and the displacement of the piston was measured to an accuracy of 0.001 mm using linear variable differential transformer (LVDT) displacement sensor. The actuator speed was set to 1mm/min, corresponding to a nominal strain rate of 0.04s^{-1} in the sample. Since almost no data regarding material densification was available before experimentation, the tests were terminated based on two conditions: first, when near-complete densification was observed in the force-displacement curve during loading, and second, when the actuator speed was no longer constant. Strains

exceeding 90% were achieved in all the quasi-static trials. The engineering stresses are calculated by dividing the applied load by the original specimen surface area, and the engineering strains are computed by dividing the specimen displacement by the original specimen height. Three trials with same loading conditions were performed to verify repeatability of the material behavior.

3.2. High strain-rate compression

The dynamic compression experiments were performed using a modified version of a split Hopkinson pressure bar (SHPB) apparatus [6], shown in Figure 3. The setup consists of a gas gun, a striker bar, an incident bar, a transmission bar, sensors, a data acquisition system, and an ultra high-speed camera. In this study, the bars were made of solid aluminium with a density of 2700 kg/m^3 and stiffness of 68.9 GPa, which were procured from McMaster-Carr. Polymeric bars have also been used in past studies in the literature to study foams [26, 27], but are recognizably more challenging to manufacture. The use of aluminium pressure bars for testing soft materials has been well documented in literature [22, 23], and we have chosen to use them in our setup because they are more easily available and less expensive. In the dynamic tests, the polymeric foam sample is sandwiched between the incident and transmission bars, and the sample end faces were lubricated with high-pressure grease so as to reduce frictional effects and to allow for easy radial expansion during compression. This setup is consistent with others in the literature [22, 24, 26 and 29].

In a SHPB experiment, a striker bar is launched from a pressurised gas gun and strikes the incident bar generating an elastic stress wave that travels through the incident bar to the sample, dynamically loading it. Due to mismatch of mechanical impedances of aluminium and the foam sample, reflected and transmitted waves are generated at the left and the right interfaces of the sample, respectively. The transmitted wave travels through the sample into the transmission bar. The incident and reflected signals are recorded by a strain gage mounted on the incident bar and

the transmitted signal is captured by a strain gage mounted on the transmission bar. The strain gages used in the setup in this study are 350Ω ± 0.3% with a gage factor of 2.130 ± 0.5% (Micro Measurements CEA-13-250UN-350). The gages are connected to their individual conditional amplifiers (Vishay InterTechnology 2310B) and a gain of 100 to 1000 is applied on the transmission gage because of the small magnitudes of transmitted stresses. The output from the conditional amplifier is fed to a Tektronix DPO2024B oscilloscope with 12-bit resolution recording at 500 MHz. Careful observation of transmitted gage raw voltage data in these experiments revealed a background noise approximately equal to ±1 micro strain, which corresponds to 20% of the measured strain at the onset of yielding (~5 micro strain). The challenges of developing SHPB systems to measure the dynamic response of foams is widely documented [17, 30], and the approaches that we pursued are consistent with those in the literature. The lengths of projectile, incident bar and transmission bars are 500, 1000 and 910 mm respectively with a diameter of 12.7 mm. The length of the bars and the relative positioning of strain gages avoid overlapping of stress waves [2], also ensuring that longer loading durations are available in order to obtain large strains in the soft foam. To prevent a sudden impact from the striker against the incident bar and to achieve better force equilibrium and constant strain rate during testing, pulse shapers made of softer material than that of bar are to be used [22, 30]. Numerous pulse-shaping trials were performed using different combinations of materials. For example, copper discs of thicknesses of 0.1 and 1mm, and different papers ranging from 100 to 240 GSM (Grams per Square Meter) were tested individually and in multiple combinations of each other. It was found that a 160 GSM paper pulse-shaper generated the desired near-rectangular shape of the input pulse, which would ensure constant strain rate and best force equilibrium throughout the experiment.

206 To compute the stress-strain responses of the material, the theory of one-dimensional wave
207 analysis in thin rods is used:

$$\sigma(t) = \frac{A_0}{2A_s} E_0[\varepsilon_i(t) + \varepsilon_r(t) + \varepsilon_t(t)] \tag{1}$$

$$\varepsilon(t) = \frac{C_0}{L_s} \int_0^t [\varepsilon_i(t) - \varepsilon_r(t) - \varepsilon_t(t)] \tag{2}$$

$$\dot{\varepsilon}(t) = \frac{C_0}{L_s} [\varepsilon_i(t) - \varepsilon_r(t) - \varepsilon_t(t)] \tag{3}$$

208 where A_0(m^2) and A_s(m^2) are the cross-sectional areas the bars and sample; $\varepsilon_i(t)$, $\varepsilon_r(t)$ and $\varepsilon_t(t)$
209 are the incident, reflected and the transmitted strain-time histories respectively; L_s(m) is the
210 thickness of the sample; E_0(N/m^2) is the Young's modulus of the bars and C_0(m/s) is the elastic
211 bar wave speed which is given by

$$C_0 = \sqrt{\frac{E_0}{\rho_0}} \tag{4}$$

212 where ρ_0(kg/m^3) is the density of bar. Since the sample size is small, it can be assumed that the
213 wave propagation effects within the specimen are negligible and this yields:

$$\varepsilon_i(t) + \varepsilon_r(t) = \varepsilon_t(t) \tag{5}$$

214 And equations (1) - (3) are simplified to

$$\sigma(t) = \frac{A_0}{A_s} E_0 \varepsilon_t(t) \tag{6}$$

$$\varepsilon(t) = -2\frac{C_0}{L_s}\int_0^t \varepsilon_r(t) \tag{7}$$

$$\dot{\varepsilon}(t) = -2\frac{C_0}{L_s}\,\varepsilon_r(t) \tag{8}$$

To validate the working of the SHPB apparatus, it is necessary that dynamic stress equilibrium be attained in the samples [29] and this is verified by equating the forces at input bar–sample ($F_{S-I}(t)$) and sample–transmission bar ($F_{I-T}(t)$) interfaces, which are given by:

$$F_{S-I}(t) = A_0E_0[\varepsilon_i(t) + \varepsilon_r(t)] \tag{9}$$

$$F_{I-T}(t) = A_0E_0\varepsilon_t(t) \tag{10}$$

Shown in Figure 4 (a) is a force balance plot between forces calculated at the incident and transmitted ends of the sample. The vertical axis represents the force experienced in Newtons (N) and the horizontal axis represents time in microseconds (μs). The forces at the input bar–sample ($F_{S-I}(t)$) and sample–transmission bar ($F_{I-T}(t)$) interfaces are represented by black and brown curves, respectively. The overlapping of the curves indicate that reasonable dynamic force equilibrium is attained within the sample.

During testing, an ultrahigh-speed camera Shimadzu HPVX-2 was used to visualize deformation features, as well as to perform strain measurements. The camera is able to capture 256 images and is triggered by a split signal from the incident strain gage. In these experiments, the camera operated at a framerate of 1 million frames per second at a resolution of 400 x 250 pixels. The camera was triggered from the incident strain gage and camera output pulses were used to correlate times between the images and the gage measurements. In the dynamic experiments, the strain was measured by tracking the displacement of two point markers on each side of the tested specimen,

one on the incident bar and the other on the transmission bar. This was done to more easily match the video images to the stress-strain curve in order to identify macroscopic deformation features that are observed in this material. Uncertainty of using the camera is approximated to lie within an error of one pixel where the initial sample size was measured to be 100 pixels in length, corresponding to a maximum strain uncertainty of 1%. A comparison of the strain rate vs. time computed for one of the experiments using the wave equations (equation (8)) and the rate vs. time computed from tracking the displacements from the high-speed camera are shown in Figure 4(b). The horizontal axis represents time in microseconds and the vertical axis represents strain rate (s^{-1}). The green curve shows the unfiltered strain rate obtained from the wave equations and the blue curve represents the strain rate history achieved using the ultrahigh speed camera. It was found that the strain rate calculated from the tracking technique lied within 3% error of the rate calculated from the wave equations for any given time after stress equilibrium has been obtained (i.e. at strains greater than 8%). Finally, three tests with same loading conditions were performed to verify repeatability of the experiments and it was found that with the same cylinder pressure, there was a variability of ~5% in the projectile velocity, which caused a variability in strain rates of 5284 to 5720 s^{-1}.

4. Experimental Results

Shown in Figure 5 is a plot of the quasi-static and dynamic stress-strain curves of the D3O LITE D, including multiple curves for experimental variability. The points 1 to 8 included on one example quasi-static and one example dynamic curve correspond to high-speed camera images that are shown and discussed later in Figure 6 and 8. The strains for which images are selected are different for the quasi-static and dynamic cases. For the quasi-static case, strains are selected at transitional points on the stress-strain curve, as well as those strains that correspond to the onset

or evolution of notable deformation features in the images. Similarly for the dynamic experiments, image locations are selected to best visualize the onset and evolution of deformation features for the higher strain rate. The results for both quasi-static and dynamic strain rates are discussed in greater detail subsequently.

4.1. Quasi-static regime

It is observed that the compressive response of the material in the quasi-static regime exhibits a typical elastomeric foam behavior with a few notable exceptions. Namely, typical foam responses have a sudden change in slope when the stress reaches elastic stress limit σ_{el}^{*} and its value is easily identifiable. However, in this material, it was found that there was a gradual transition from the elastic regime to the plateau regime beginning at a strain of 2% and plateauing at approximately 6% strain, which does not yield a specific value of σ_{el}^{*}. Therefore, average stress over the specified strain range between 4.6 to 5.2% was calculated, where an initial increase in slope is observed, and σ_{el}^{*} was measured to be 120 ± 55 kPa over this range. In the figure, the curve then starts to plateau at around 6% at a stress of about 145 kPa, indicating the start of post-elastic collapse regime. From this point, the sample continues to harden with a linearly increasing hardening rate until a strain of ~60% is reached within the sample. The sample then starts to densify at an increasing rate until a strain of ~83% at a stress of 5.05 ± 2.1 MPa is reached in the sample, at which point the sample starts to densify rapidly. It is also observed that there was a sudden increase followed by a gradual decrease in the hardening rate at this strain. The strain of ~83% coincides with the porosity of the material, and so this hardening behavior likely corresponds to near-complete pore collapse. At this point, the porosity is completely crushed out and the foam tends to behave linearly like the elastic part of the compressive behaviour of the parent bulk polymer [17, 18]. To understand the variability in the material behavior and consistency of the mechanical

properties obtained from the experiments, three stress-strain curves under the same strain-rate and loading conditions were obtained, and these are also shown in Figure 5. It can be seen that below strains of 70%, the stress-strain curves overlap within 4 % error, and the variability observed after 70% strain are related to the differences in material composition, individual sample density and microstructure. For a given sample, the pore collapse strain ranges between 114 and 126 kPa, while the stress variability at 90% strain can range between 28 and 44 MPa.

To better understand the failure mechanisms that influence the stress-strain responses, we present images taking using a high-speed camera during quasi-static testing (Figure 6). The image numbers correspond to the numbers shown on the quasi-static stress-strain curves in Figure 5. Image 1 shows the start of the experiment at 0% strain, and is shown for reference. From image 2, it is observed that from a strain of 0 –12%, there is no noticeable lateral deformation. This suggests that the Poisson's ratio may be negligible throughout the elastic regime and early plateau. This is consistent with observations by Liu et al. [26] for their polymeric foam (acquired from Airbus). As seen from images 3 through 6, very low lateral deformation is observed corresponding to a Poisson's ratios less than 0.02; no clear deformation features are visible on the material surface. In image 7, visually distinguishable deformation appears in lateral direction at a strain of ~72%, and densification begins to occur ending the plateau regime. Finally, image 8 is taken at a strain of ~84%, where considerable lateral expansion is observed and at strains higher than this, the sample moves out of the camera's field of focus. The final lateral deformation was measured at ~84% and the corresponding Poisson's ratio was calculated to be ~0.11±0.02. All of lateral deformation measurements were performed using ImageJ. Throughout the range of strains, it was observed that there were no distinctive macroscopic deformation features on the imaged surface, which are contrasted with dynamic results next.

300 *4.2. Dynamic Regime*

301 Prior to discussing the stress-strain responses for the dynamic experiments in Figure 5, we first
302 discuss the effect of filtering levels on the strain-strain curves presented in Figure 7. In our
303 experiments, data from the oscilloscope was sampled at 500 MHz (fixed oscilloscope setting), and
304 filtering techniques were explored to better visualize the raw data and contrast it with the quasi-
305 static experimental trends (e.g., features like the elastic collapse, densification). Some level of
306 filtering of high strain-rate data appears to be frequently used in the published literature on foams
307 [17, 22, 24, 30] (based on smoothness of curves), with limited discussion for filtering approaches
308 (e.g., frequency-based filters [31]). To explore the effect filtering, we use a first order Savitzky–
309 Golay (SG) filter in Matlab, which helps increase the signal-to-noise ratio without greatly
310 distorting the signal. The smoothing is achieved using a process called convolution, which fits
311 segments of adjacent data points with a low-degree polynomial by the method of linear least
312 squares. The choice of this filter, we believe, allows us to maintain the general trends and stress
313 magnitudes in the data (which we explore here). In this exercise, we show the effect of different
314 filtering levels for one of the dynamic experiments in Figure 7. Here, we selected to apply filtering
315 levels beginning at filtering segment sizes corresponding to 0.05% strain and increasing by 0.05%
316 strain up to 1%, which we believed to represent low degrees of filtering when first selected. In the
317 figure, we show an unfiltered curve, and curves for filtering levels for segment sizes of 0.2%
318 (corresponding to 180 points), 0.5% (corresponding to 450 points), and 1% (corresponding to 900
319 points). The black curve shows the unfiltered data, followed by the red curve which corresponds
320 to a segment size of 0.2% strain. It can be seen that the red curve overlaps over the black curve in
321 all ranges of strain suggesting that both magnitudes and trends are preserved at this level of
322 filtering. Increasing the strain segment size to 0.5% strain leads to a three fold reduction in elastic

collapse stress, as well localized distortion of the general trend at low strains which are represented by the light grey curve. The dark grey curve represents filtering corresponding to a strain segment size of 1% and it can be observed the overall trend is captured but stress magnitudes are reduced drastically with increasing segment sizes. These values demonstrate the outcome of the analysis. Namely, it was observed that increasing the strain segment size to greater than 0.25% strain leads to distortions of the general trend and decreased stress magnitudes, and so a size of 0.2% strain was selected because this lied within acceptable filtering levels.

Now that filtering has been explored, we return to describe the stress-strain response of the foam in Figure 5 for strain rate of 5284 to 5720 s^{-1}. For the dynamic case, the linear-elastic regime spans up to a strain of ~1% and the elastic collapse stress σ_{el}^{*} is calculated to be approximately equal to 243 ± 47 kPa. In our experiments, the transition from the elastic regime to the plateau regime begins at a strain of 0.8% and plateaus at around 1.5% strain. We note here that the stress in the sample has not yet equilibrated (see Figure 4(a)), and care should be given to interpretation of these values as discussed in Song et al. [30]. In our tests, a constant strain rate and force balance is achieved in the sample at ~ 8%. In the dynamic tests, the stress in the sample continues to rise between 8% (stress of 280 ± 25 kPa) and 45% (460 ± 40 kPa) at a constant rate in this log-linear representation. This linear rise corresponds to an initial plateau regime. Interestingly, there is a secondary hardening regime beyond 45% strain that increases logarithmically until a strain of 81 to 83% (22.5 ± 4.0 MPa). This pronounced hardening rate corresponds to densification of the foam sample. Again, this likely corresponds to pore collapse in the sample, albeit at a slightly less strain value than observed in the quasi-static experiments. After this point, there is an inflection in the curve at ~83%, which is believed to correspond to complete densification. After a strain of ~81%

is achieved within the sample, the material hardens more rapidly than the quasi-static tests, and this likely corresponds the behavior of the parent material.

To better understand the hardening regimes, we present ultra-high-speed camera images taken during deformation (Figure 8). In this D3O LITE D foam, some unique macroscopic deformation features are observed. Shown in Image 1 of Figure 8 is a reference image taken at 0 % strain for the dynamic experiments. Image 2 corresponds to strains of around 8 – 10%, where small band-like features begin to appear. Image 3 shows the sample at 18 to 20% strains where these features become more visually apparent as indicated by the red lines in the image. Note the red lines are used to highlight the location of these vertical bands and this meant to ease the reader in visualizing the growth of the bands in subsequent images. These band-like deformation features are termed as "localizations" hereafter. It was observed that at strains between 20 – 35 % (Image 4), a greater number of localization features appear to nucleate, and this corresponds to the near-horizontal plateau in the log-linear regime of the stress-strain curve in Figure 5. These localization features continue to nucleate and grow perpendicular to the compressive loading direction until strains of 42 – 45% are reached within the sample, shown in image 5. After 45% strain, no more new nucleations are observed in the ultra-high-speed camera images, and at strains beyond 45%, the localizations begin to coalesce with each other until they span the entire length of the sample at 75 to 80 % strain (shown in images 6 to 8). In the dynamic experiments, lateral expansion was measured at the aforementioned strains using ImageJ and a constant expansion rate was observed leading to a Poisson's ratio of ~0.095 at a strain of 76%. After strains of 85% – 90% are reached, the sample expands out of the field of focus of the camera.

5. Discussion

This paper investigated the compressive failure of a shear-thickening polymeric foam for quasi-static and dynamic conditions. It is important to better understand the behavior of these materials since this class of foams are currently being employed in energy absorption equipment (e.g., helmet liners for US team sports such as Football, Baseball and Ice Hockey, as well as protective inserts for Motorcycle jackets) and also in some military applications [34]. Limited data on these materials, and shear thickening foams in general, exist in the literature, and so we believe that this paper makes contributions towards better understanding how microstructural features and lengths scales of these types of foams may be related to quasi-static and dynamic compressive failure. In what follows, we discuss the results of this foam in the context of our general understanding of how polymeric foams behave.

To summarize the results and discussion of this paper, we show Table 2 which consists of the stress regimes, Poisson's ratio measurements(μ) and the dominating failure mechanisms corresponding to that given ranges of strains. This table also provides image numbers corresponding to images from high speed camera for quasi-static case, and similarly for ultra-high speed camera images for the dynamic case from Figures 6 and 8 respectively, so that it is easier for the reader to visualize camera images while referring to the table.

First, we correlate commonly known deformation mechanisms to the stress-strain curves of our D3O LITE D foam in quasi-static and dynamic conditions (Figure 5). Generally, three different phases of deformation are observed during compressive failure of polymeric foams [17, 21 and 32]. The first phase is linear-elastic regime, where the stress-strain response follows Hooke's law and the strain is completely recoverable. For polymeric foams, the linear-elastic limit is limited to small strains, typically less than 5% strain [24, 30]. It is to be noted that elastomeric foams can

391 undergo much higher strains than these and the deformation can still be mostly recoverable, but is
392 non-linear [32]. The second phase is characterized by non-linear elasticity, where the material
393 continues to plateau at a relatively constant stress, known as the elastic collapse stress σ_{el}^{*}. This
394 property of foams is exploited for energy-absorbing applications [21]. The third and final phase of
395 deformation is known as densification, where the foam begins to respond like a compacted solid
396 [17, 24]. For semi-closed cell foams, these deformation and failure mechanisms are usually more
397 complicated than fully open or closed celled foams due to the presence of higher number of face
398 edges where damage can nucleate [31]. Each of the three phases is explained in the context of our
399 material hereafter with a main focus on dynamic response.

400 In our dynamic experiments, the linear elastic regime extends to about 1 – 1.5% strain and in this
401 regime all stresses are carried by only the cell ligaments, which show small regions of buckling,
402 directly contributing towards the stiffness of the material. There is no failure in the linear elastic
403 regime and the strains are fully recoverable. Similar mechanisms are observed in the quasi-static
404 case as well, but at different elastic strain limits as discussed earlier. In our dynamic experiments,
405 the post-elastic collapse behaviour begins at around 1.5% strain and is dominated by buckling of
406 both cell edges and faces. This mechanism spans the entire inelastic regime. In the first plateau,
407 permanent bending of cell walls dominates up to a strain of ~45% alongside large-sized buckling
408 regions near the cell walls. In the second plateau region following the permanent deformation of
409 the cell walls, the cell faces begin to rupture followed by tearing of the cell edges at strains of
410 ~62%, and this process occurs progressively in the rest of the plateau regime. Initial damage is
411 observed at the near-closed cells, and these cells begin to rupture at the strain nearing the end of
412 plateau, reaching to the point of densification, which begins at around 81% strain. In our quasi-
413 static experiments, the post-elastic collapse behaviour begins at ~6% strain and hardens linearly

until ~60% strain after which gradual densification is observed up to strains of ~83%. Similar failure mechanisms that have been discussed for dynamic conditions are activated in quasi-static conditions at similar strains except for that of complete densification. A deviation from typical foam behaviour [13, 17, 18, 21, 32 and 33] in our experiments was that the hardening rate of the plateau stress was found to be more than an order of magnitude higher than the elastic collapse stress in quasi-static rate and almost two orders of magnitude higher in dynamic strain rate conditions. At these high strains, the opposing cell walls have been observed [17] to crush together and cell wall material is itself compressed and complete densification is observed. It is to be noted that each failure mechanism, once activated continues to remain active until failure.

After densification, complete pore collapse is observed. In the quasi-static case for our experiments (Figure 5), there was an inflection at the curve around 87 ± 3 %, and we believe that is likely related to complete pore collapse. In the dynamic case, the inflection was observed around 83 ± 3%, which was lower than the quasi-static. The formation of the structural-scale vertical localizations are believed to be responsible for the lower pore collapse strain in the dynamic case as a result of these localization features consuming porosity during their nucleation, growth, and coalescence. This factor needs to be considered in any dynamic failure modelling of foams where large strains at high strain rates are experienced because the formation of these localizations govern the hardening rates in the plateau regime, which in turn are responsible for material response at high strain rates. Lastly, after complete pore collapse, post pore collapse hardening was observed. Post pore collapse hardening rates in both quasi-static and dynamic cases are found to be greater than the rate of densification in their respective cases. The dynamic post pore collapse hardening rate is observed to be greater than the quasi-static post pore collapse hardening rate. This is explained by the general rate dependency behaviour in bulk polymers [22] at high strains given

437 when the entire porosity in the foam is crushed out, the sample essentially behaves like a bulk
438 polymer material. Although not explicitly reported by the authors, similar effects are observed in
439 other materials [17, 32]. After this point, at very large compressive strains of over 85%, the sample
440 under the given mechanical loading tends to behave like material response of the parent material.
441 It is to be noted that the vertical axis shown in Figure 5 is of log scale and these hardening rates
442 may not be as easily visualized in the stress-strain curves presented in the paper.

443 The localization behavior foams advertised as shear thickening is not currently understood, but is
444 likely related to some combination of chemical composition and structure (held proprietary by the
445 manufacturer), the microstructure (in terms of pore size and wall thickness), and the strain energy
446 that is available for failure (assessed via mechanical testing and stress-strain response). Additional
447 experiments are needed to better understand the mechanisms for nucleation and growth of the
448 localization features (e.g., interrupted compression or impact experiments coupled to X-Ray
449 imaging of internal microstructure features), and energy-based or computational models are
450 required to confirm experimental observations.

451 With this in mind, we briefly explore potential reasons for the observed localization features in
452 this foam, which, to the knowledge of the authors, are unique to this as-advertised shear thickening
453 foam. As mentioned, these localization features are believed to be a consequence of chemical
454 composition and structure, and the microstructure (i.e., in terms of pore size and wall thickness).
455 In this discussion, we focus on the microstructural contributions since the chemical composition
456 and structure information (and foam manufacturing process) is proprietarily held by the
457 manufacturer. We link the localization features to instabilities that lead to buckling of cell walls
458 perpendicular to the compressive loading direction. The onset of these instabilities are believed to
459 be related to the relative sizes of the pores and the wall thickness, where relatively large pore sizes

460 results in relatively higher localized stresses concentrations, and relatively thinner walls are more
461 susceptible to collapse under these relatively higher stresses. In this D3O LITE D material, the
462 ratio of pore sizes (average of 82 ± 26 μm) to wall thickness (average of 8.3 ± 4.5μm) is 4.3 to 28
463 (average 9.8). In other materials, where SEM images are available, we see wall thickness to pore
464 sizes ratios of ~0.025 and ~0.002 [18, 24], and perhaps these ratios play a role in the unique
465 behavior of the Lite D foam. It is, however, to be noted that these materials have different
466 compositions, and this form of foam microstructure with its unique wall thickness to pore size
467 ratio, pore shapes, distributions, and locations of unexpanded polymer is found to be unique to
468 D3O LITE D when compared to other images of foam microstructures in literature [11, 18, 24 and
469 31].

470 **6. Conclusion**

471 The compressive response of D3O LITE D dilatant foams under quasi-static strain rate of 0.04 s^{-1}
472 and dynamic strain rate of 5284 to 5720 s^{-1} has been studied. Experimental methods for
473 characterizing and studying the dynamic response of foams have been established and have found
474 to reconcile with traditional experimental techniques. Comprehensive insights into compressive
475 behavior of shear thickening foams are provided, which is relatively an unexplored area of research
476 despite current use of these materials in many applications. Most notably, under dynamic loading
477 conditions, unique macroscopic localization features are observed in the D3O LITE D foam under
478 investigation in this paper, which do not appear at quasi-static rates or in any high rate testing of
479 other polymeric foams (to the knowledge of the authors). This data can be used for modelling the
480 observed localizations as a unique failure mechanism in mechanism-based modelling approach to
481 predict material response. More studies at intermediate strain rates are required to identify the
482 threshold strain rate for these localizations and to study the effect of these localizations on shear

thickening behavior. As this is the first time that the D3O LITE D foams have been characterized in this way, we believe these experimental results will also serve as a good starting point for impactful modelling [11, 33]. The results of the tests performed and the future tests will be put together to make models to predict the effect of microstructure, strain rate and localizations on the compressive response of shear thickening foams.

7. Acknowledgements

This research was sponsored by the Army Research Laboratory and was accomplished under Cooperative Agreement Number W911NF-16-2-0083. The views and conclusions contained in this document are those of the authors and should not be interpreted as representing the official policies, either expressed or implied, of the Army Research Laboratory or the U.S. Government. The U.S. Government is authorized to reproduce and distribute reprints for Government purposes notwithstanding any copyright notation herein. We also greatly acknowledge the in-kind support of Defence Research and Development Canada. We also thank Bernie Faulkner of Department of Mechanical Engineering, University of Alberta for his help with experimental setup and Christopher S Meredith of Army Research Laboratory for his insightful discussions.

List of Tables

List of Figures

length scales are denoted on the bottom-left corner of each image. Large-scale linear deformations are not observed in the quasi-static case, like the dynamic case.

Figure 7. Plot showing effect of different filtering levels on stress magnitudes and global trends of dynamic compressive response of D3O LITE D foam. The red curve is indicative of acceptable filtering level with a strain segment size of 0.2%. The light grey and dark grey are example curves at larger segment sizes of 0.5% and 1% respectively, that show distortions from original response indicating over-filtering.

Figure 8. Time-evolved dynamic compression failure of the D3O at 5465 s^{-1} using Split Hopkinson Pressure Bar apparatus. Inter-frame strains are denoted at the bottom-left corner of each image and specimen length scales are denoted on the top-right corner of each image. The red lines in image 3 emphasize larger-scale vertical localization bands that start to form in this material at approximately 10% strain. This corresponds to log-linear region in the red line in Figure 5.

Tables

Table 1. Manufacturer's listed properties for D3O LITE D.

Material	Density Range	Hardness	Tensile Strength	Split Tear Strength	Compressive Strength	Flexural Modulus	Water Absorbency
D3O Lite D	200 - 220 Kg/m^3	60 Asker C	2.2 MPa	2.9 N/mm	190 kPa	5.59 MPa	1 %
Test Method	ISO 845: 2009	DTS004	ISO 1798: 2008	SATRA TM65	ASTM D3575-14D	DTS052	ISO 62 : method 1

573 **Table 2.** Summary table showing the stress regime, Poisson's ratio (μ) and the dominating failure
574 mechanism corresponding to the given ranges of strains. It is to be noted that each failure
575 mechanism, once activated continues to remain active until failure. Also, image numbers
576 corresponding to that of Figure 6 are provided for high speed camera images for quasi-static case,
577 and similarly for ultra-high speed camera images for the dynamic case with respect to Figure 8.

Strain range	**Quasi-static**				**Dynamic**				
	#	**Stress Regime**	**μ**	**Failure mechanism**	**#**	**Stress Regime**	**μ**	**Failure mechanism**	**Deformation features**
0 – 10	1	Linear elastic	0	Elastic Collapse	1	Linear elastic	0	Elastic Collapse	None
10 – 20	2	Plateau	0	Buckling	2	First Plateau	0.012	Buckling	Nucleations begin
20 – 30	3	Plateau	0	Buckling	3	First Plateau	0.025	Cell Wall Bending	Higher Nucleations
30 – 40	4	Linear Hardening	0.003	Cell Wall Bending	4	First Plateau	0.038	Cell Wall Bending	Nucleations stop
40 – 50	5	Linear Hardening	0.006	Cell Wall Bending	5	Secondary Hardening	0.052	Pore Collapse	Localizations grow
50 – 60	6	Linear Hardening	0.020	Pore Collapse	6	Secondary Hardening	0.067	Pore Collapse	Growth & Coalescence
60 – 70	6	Densification	0.020	Pore Collapse	7	Densification	0.081	Tearing	Growth & Coalescence
70 – 80	7	Densification	0.110	Tearing	8	Densification	0.095	Complete pore collapse	Full sample length
80 – 90	8	Complete Densification	-	Complete Densification	-	Complete Densification	-	Post-pore collapse	-

Figures

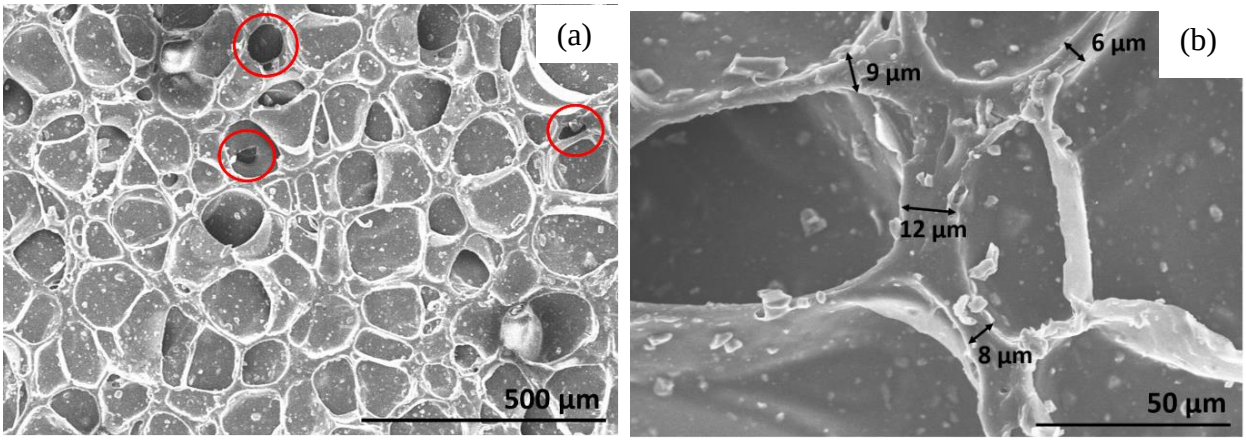

Figure 1. (a) Scanning Electron Microscope (SEM) Micrograph of D3O LITE D at 100 x magnification showing microstructure dominated by fairly circular pores of varying sizes with rare instances of semi-open pores represented by red circles. **(b)** SEM Micrograph at 600 x magnification showing sample wall thickness measurements. The bright features that are prominently visible in this cross-section are a result of additives/unexpanded bulk polymer. The length scales are denoted on the bottom-right corner.

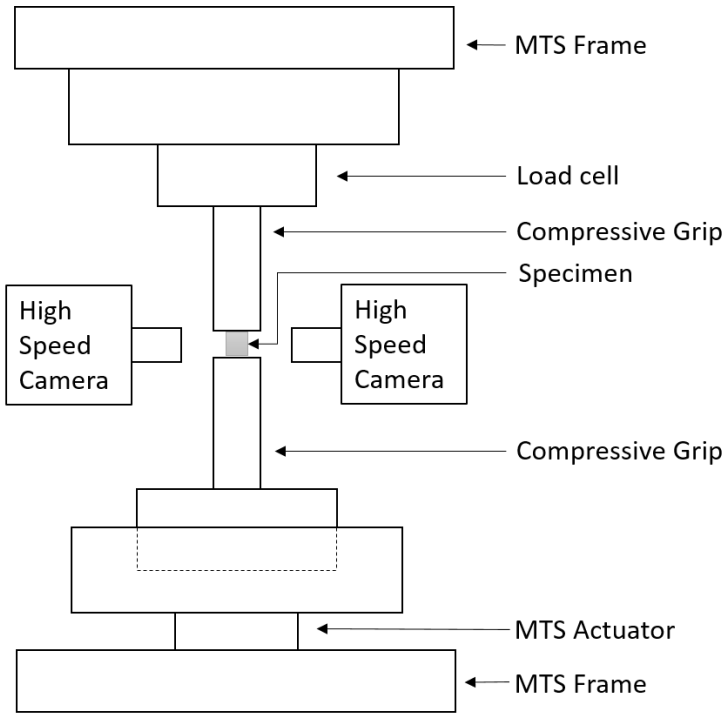

Figure 2. Schematic diagram of the MTS experimental setup combined with two high-speed cameras perpendicular to each other facing the sample to aid in Poisson's ratio measurement.

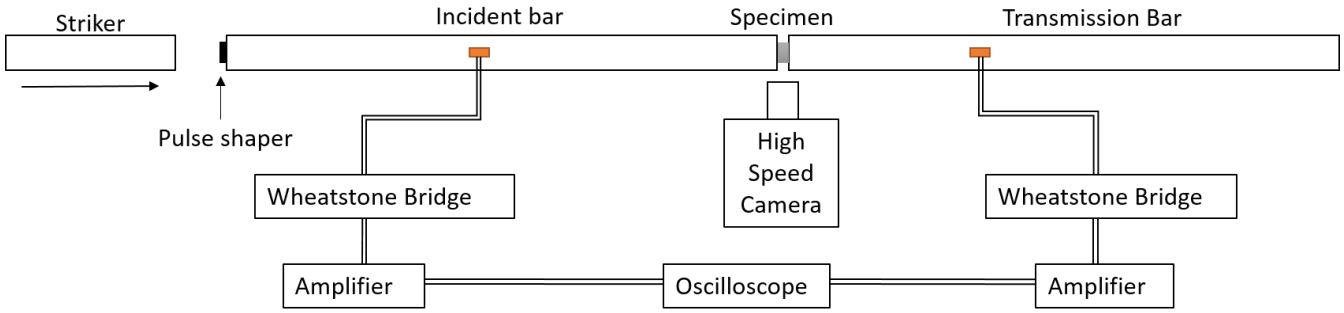

Figure 3. Schematic diagram of the Aluminium Split Hopkinson Pressure Bar experimental setup combined with Ultra-high speed camera for strain measurement and visualization of deformation features.

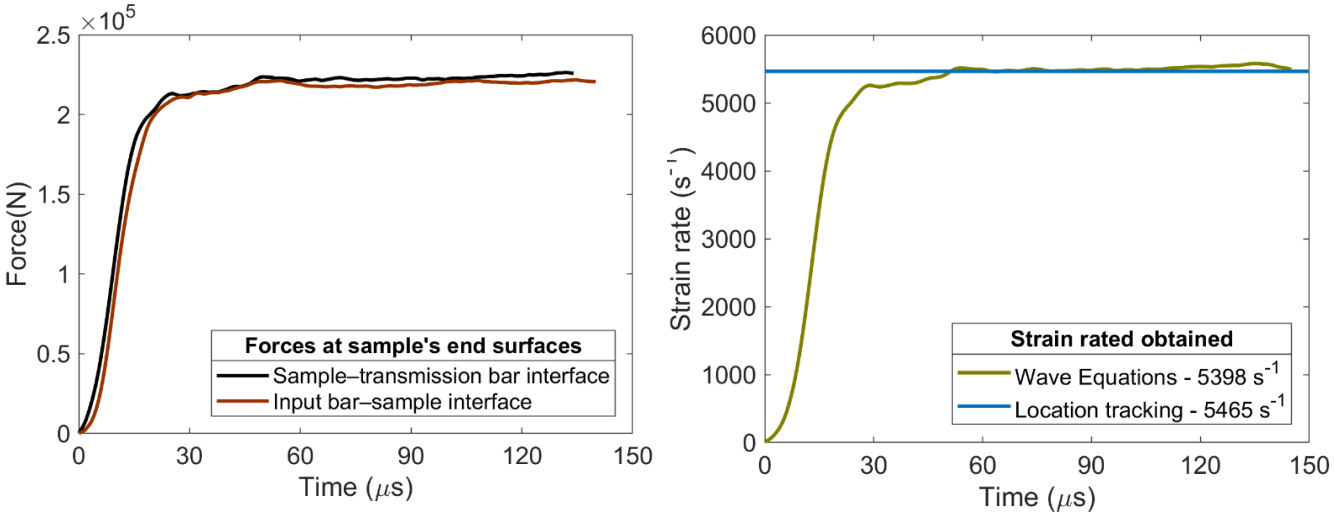

Figure 4. (a) Plot showing dynamic force balance between foam sample's end surfaces during dynamic compressing testing using Split Hopkinson Pressure Bar. **(b)** Strain rate history of the sample observed during dynamic compression using wave equations, and using location tracking technique which tracks markers on Ultra-high speed camera images to calculate strain and strain rate. Both based on individual MATLAB programs.

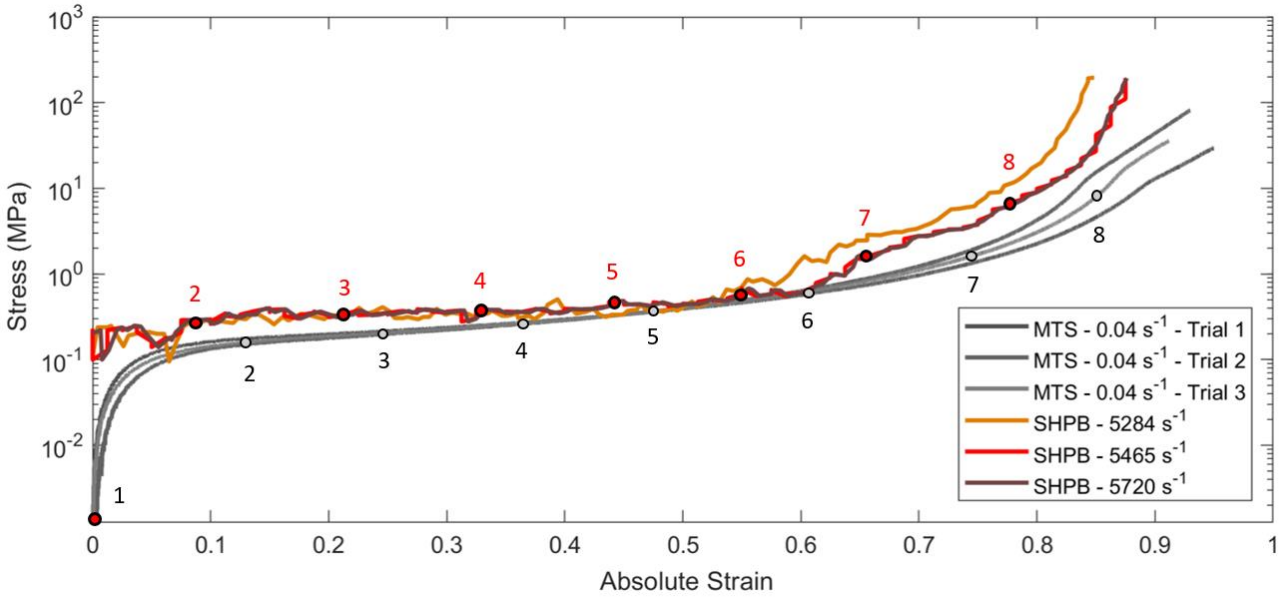

596 **Figure 5.** Stress-strain curves from quasi-static and dynamic compression experiments. Black
597 points on the quasi-static curve are represented by high-speed camera images in Figure 6; Red
598 points on the dynamic curve are represented by ultra-high speed camera images in Figure 8.

599

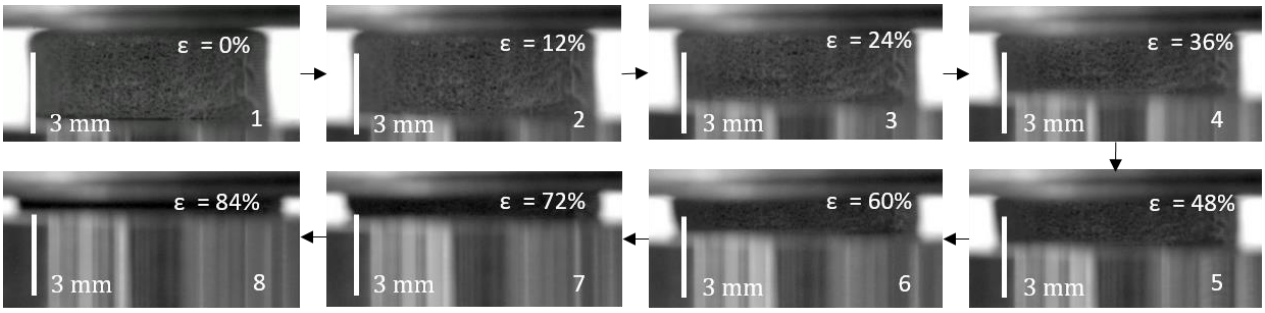

600 **Figure 6.** Time-evolved quasi-static compression failure of the D3O foam at 0.04 s^{-1} using MTS
601 810 apparatus. Inter-frame strains are denoted at the top-right corner of each image and specimen
602 length scales are denoted on the bottom-left corner of each image. Large-scale linear deformations
603 are not observed in the quasi-static case, like the dynamic case.

604

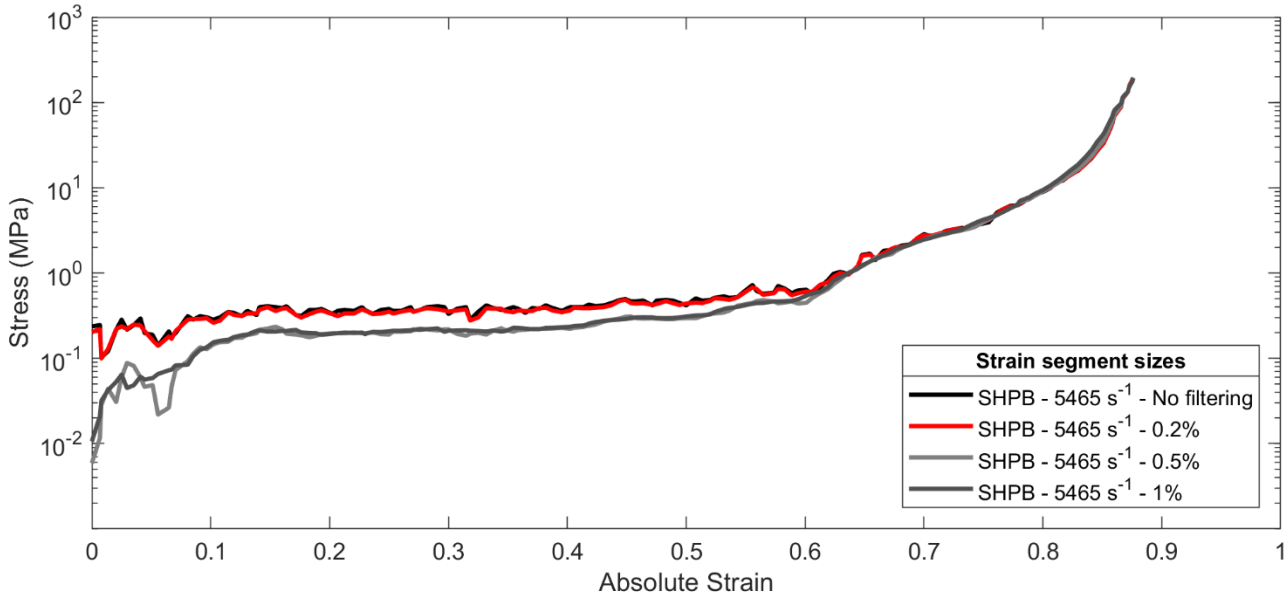

Figure 7. Plot showing effect of different filtering levels on stress magnitudes and global trends of dynamic compressive response of D3O LITE D foam. The red curve is indicative of acceptable filtering level with a strain segment size of 0.2%. The light grey and dark grey are example curves at larger segment sizes of 0.5% and 1% respectively, that show distortions from original response indicating over-filtering.

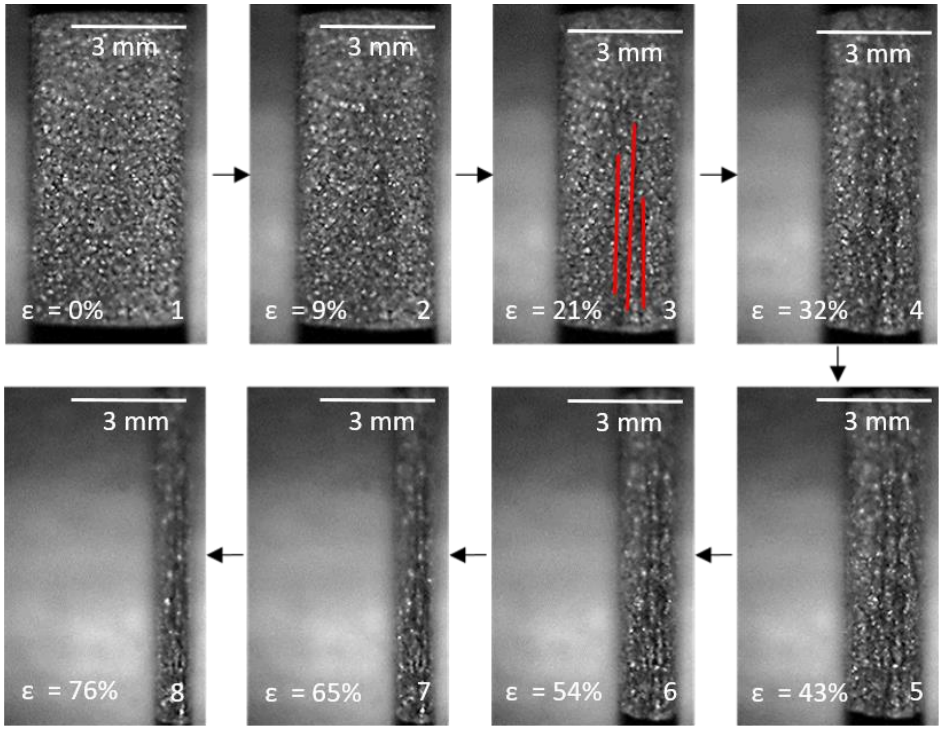

Figure 8. Time-evolved dynamic compression failure of the D3O at 5465 s^{-1} using Split Hopkinson Pressure Bar apparatus. Inter-frame strains are denoted at the bottom-left corner of each image and specimen length scales are denoted on the top-right corner of each image. The red lines in image 3 emphasize larger-scale vertical localization bands that start to form in this material at approximately 10% strain. This corresponds to log-linear region in the red line in Figure 5.

References

[1] *D3O® FORMABLE FOAMS* (2016). Retrieved from https://www.d3o.com/wp-content/uploads/2016/08/D3O-Formable-Foams.pdf. Accessed 22 June 2017.

[2] G. T. Gary. Classic split-hopkinson pressure bar testing. Mechanical testing and evaluation, metals handbook. American Society for Metals, 2000. Materials Park, Ohio, 8. 462–476

[3] R. Clamroth. Determination of viscoelastic properties by dynamic testing. Polym. Test., 1981. 263–286.

[4] J. A. Harris. Dynamic testing under nonsinusoidal conditions and the consequences of nonlinearity for service performance. Rubber Chem. Technol., 1987. 870–887.

[5] M. A. Meyers. Dynamic Behavior of Materials. John Wiley & Sons, 1994.

[6] H. Kolsky. An investigation of the mechanical properties of materials at very high rates of loading. Proc. Phys. Soc. London, B62:676–700, 1949.

[7] R. C. Progelhof. Impact measurement of low-pressure thermoplastic structural foam. In Proceedings of Instrumented Impact Testing of Plastics and Composite Materials, pages 105–116, Houston TX, March 11-12, 1986. ASTM. 105–16

[8] D. F. Sounik, P. Gansen, J. L. Clemons, and J. W. Liddle. Head-impact testing of polyurethane energy-absorbing (ea) foams. SAE Trans. J. Mater. & Manu., 1997 ;106:211–20.

[9] G.T. Gray III, W. Blumenthal, Split Hopkinson pressure bar testing of soft materials, ASM Handb. Mech. Test. Eval. 8 (2000) 488-496.

[10] S. T. Marais, R. B. Tait, T. J. Cloete, and G.N. Nurick. Material testing at high strain rate using the split hopkinson pressure bar. Latin Amer. J. Solids Struct., 2004.

[11] Bouix, R., Viot, P., & Lataillade, J. L. (2009). Polypropylene foam behaviour under dynamic loadings: Strain rate, density and microstructure effects. International Journal of Impact Engineering, 36(2). 329-342.

[12] Ajdari, A., Nayeb-Hashemi, H., & Vaziri, A. (2011). Dynamic crushing and energy absorption of regular, irregular and functionally graded cellular structures. International Journal of Solids and Structures, 48(3-4), 506–516.

[13] Avalle, M., Belingardi, G., & Montanini, R. (2001). Characterization of polymeric structural foams under compressive impact loading by means of energy-absorption diagram. International Journal of Impact Engineering, 25(5). 455-472.

[14] Cernak, I., Merkle, A. C., Koliatsos, V. E., Bilik, J. M., Luong, Q. T., Mahota, T. M., … Ahmed, F. A. (2011). The pathobiology of blast injuries and blast-induced neurotrauma as identified using a new experimental model of injury in mice. Neurobiology of Disease, 41. 538-551.

[15] Kiernan, S., Cui, L., & Gilchrist, M. (2009). Novel Energy Absorbing Materials with Applications in Helmeted Head, 1–4.

[16] Nemat-Nasser, S., Kang, W. J., McGee, J. D., Guo, W. G., & Isaacs, J. B. (2007). Experimental investigation of energy-absorption characteristics of components of sandwich structures. International Journal of Impact Engineering, 34(6). 1119-1146.

[17] Ouellet, S., Cronin, D., & Worswick, M. (2006). Compressive response of polymeric foams under quasi-static, medium and high strain rate conditions. Polymer Testing, 25(6). 731-743.

[18] Saha, M. C., Mahfuz, H., Chakravarty, U. K., Uddin, M., Kabir, E., & Jeelani, S. (2005). Effect of density, microstructure, and strain rate on compression behavior of polymeric foams. Materials Science and Engineering A, 406. 328-336.

[19] Wang, L., Labibes, K., Azari, Z., & Pluvinage, G. (1994). Generalization of split Hopkinson bar technique to use viscoelastic bars. International Journal of Impact Engineering, 15(5). 669–86.

[20] Santa Maria, J. A., Schultz, B. F., Ferguson, J. B., Gupta, N., & Rohatgi, P. K. (2014). Effect of hollow sphere size and size distribution on the quasi-static and high strain rate compressive properties of Al-A380-Al2O3 syntactic foams. Journal of Materials Science, 49(3). 1267–1278.

[21] Di Landro, L., Sala, G., & Olivieri, D. (2002). Deformation mechanisms and energy absorption of polystyrene foams for protective helmets. Polymer Testing, 21(2). 217–228.

[22] W. Chen, F. Lu, M. C. (2002). Tension and Compression Tests of Two Polymers Under Quasi-Static and Dynamic Loading. Polymer Testing, 21. 113-121.

[23] W. Chen, B. Zhou. (1998). Constitutive behavior of Epon 828/T- 403 at various strain rates, Mechanics of Time-Dependent Materials 2. 103-111.

672 [24] Ouellet, S., Cronin, D. S., Moulton, J., & Petel, O. E. (2013). High rate characterization of
673 polymeric closed-cell foams: Challenges related to size effects. Conference Proceedings of the
674 Society for Experimental Mechanics Series, 1. 21-28.

675 [25] Viot P, Beani F. Comportement de mousses polyme`res en compression dyna- mique.
676 Revue des Composites et des Mate´riaux Avance´ s, vol. 13(no. 3); 2003.

677 [26] Liu, J., Saletti, D., Pattofatto, S., & Zhao, H. (2014). Impact testing of polymeric foam using
678 Hopkinson bars and digital image analysis. Polymer Testing, 36.

679 [27] Liu, Q., & Subhash, G. (2006). Characterization of viscoelastic properties of polymer bar
680 using iterative deconvolution in the time domain. Mechanics of Materials, 38(12). 1105-1117.

681 [28] JD Hogan, L Farbaniec, N Daphalapurkar, KT Ramesh. On Compressive Brittle
682 Fragmentation. Journal of the American Ceramic Society 99 (6), 2159-2169.

683 [29] Irausquín, I., Pérez-Castellanos, J. L., Miranda, V., & Teixeira-Dias, F. (2013). Evaluation
684 of the effect of the strain rate on the compressive response of a closed-cell aluminium foam using
685 the split Hopkinson pressure bar test. Materials and Design, 47, 698–705.

686 [30] Song, B., Chen, W. W., Dou, S., Winfree, N. A., & Kang, J. H. (2005). Strain-rate effects on
687 elastic and early cell-collapse responses of a polystyrene foam. International Journal of Impact
688 Engineering, 31(5), 509–521.

689 [31] Gao, K., van Dommelen, J. A. W., & Geers, M. G. D. (2016). Microstructure
690 characterization and homogenization of acoustic polyurethane foams: Measurements and
691 simulations. International Journal of Solids and Structures, 100–101, 536–546.

692 [32] Cronin, D. S., & Ouellet, S. (2016). Low density polyethylene, expanded polystyrene and
693 expanded polypropylene: Strain rate and size effects on mechanical properties. Polymer Testing,
694 53, 40–50.

695 [33] Avalle, M., Belingardi, G., & Ibba, A. (2007). Mechanical models of cellular solids:
696 Parameters identification from experimental tests. International Journal of Impact Engineering,
697 34(1), 3–27.

698 [34] *Morgan and D3O Create World's Most Advanced Helmet for Defence Sector*. Retrieved
699 from http://www.morganadvancedmaterials.com/en-gb/graduate-hub/morgan-news/morgan-and-
700 d3o-create-world-s-most-advanced-helmet-for-defence-sector/. Accessed 25 November, 2017.

701 [35] Subhash, G., Liu, Q., & Gao, X. L. (2006). Quasistatic and high strain rate uniaxial
702 compressive response of polymeric structural foams. International Journal of Impact
703 Engineering, 32(7), 1113–1126.